Optics Letters

Compact underwater single-photon imaging lidar

Mingjia Shangguan,[1,2,*] Ye Li,[1,2] Yican Mo,[1,2] Jun Wang,[3,4] and Tao Huang[1,2]

[1]State Key Laboratory of Marine Environmental Science, College of Ocean and Earth Sciences, Xiamen University, Xiamen 361102, China
[2]Key Laboratory of Underwater Acoustic Communication and Marine Information Technology of the Ministry of Education, Xiamen University, Xiamen 361005, China
[3]College of Meteorology and Oceanography, National University of Defense Technology, Changsha 410073, China
[4]wwjj103@nudt.edu.cn
*mingjia@xmu.edu.cn

Received 4 February 2025; revised 19 February 2025; accepted 25 February 2025; posted 27 February 2025; published 10 March 2025

Underwater target imaging is important for marine resource exploration, underwater navigation, and related fields. Lidar, with its high angular resolution, excellent depth resolution, and long-distance 3D imaging capabilities, has become an essential tool for target imaging. However, the strong absorption and scattering properties of water, along with the constraints of lidar power consumption and system size, present significant challenges for high-performance lidar systems that are deployable in underwater and even deep-sea environments. To address these challenges, this work proposes and demonstrates a compact, all-fiber underwater imaging lidar. This lidar incorporates highly sensitive single-photon detection technology and features a cylindrical design with a diameter of 0.18 m and a length of 0.68 m. To achieve miniaturization, time-division multiplexing based on fiber arrays is employed, enabling the imaging of small underwater targets using two single-pixel detectors and a two-channel acquisition card. Additionally, an algorithm is introduced to effectively extract and subtract scattering signals from suspended particles in the water column. Tank experiments confirm that the system achieves imaging distances exceeding 10 times the optical attenuation length, and its distance and lateral resolutions are validated using step and stripe targets. With its outstanding performance and broad application potential, this compact lidar system is poised to complement imaging sonar and play a key role in underwater target monitoring and search operations.

https://doi.org/10.1364/OL.557195

Underwater target imaging is vital for applications such as navigation, resource exploration, and environmental monitoring [1]. Current technologies primarily include camera-based systems and sonar. Camera systems, though enhanced by machine learning for target recognition [2], provide only 2D images and are limited to a range of 1–3 times the optical attenuation length (AL). Sonar, on the other hand, offers long-range imaging, with multibeam sonar achieving dm-level resolution [3], and synthetic aperture sonar reaching cm-level resolution [1]. However, synthetic aperture sonar has a near-field blind spot and, like camera systems, lacks depth information, requiring integration with other sonar systems or algorithms to obtain depth or distance data [4,5].

Lidar has emerged as a crucial complement to sonar and imaging technologies due to its high angular resolution, excellent depth resolution, and long-distance 3D imaging capabilities. To enhance underwater target imaging distance and resolution, several emerging technologies have been proposed, including optical frequency comb technology [6], ghost imaging [7], large-field streak tube technology [8], modulated picosecond Q-switched lasers [9], spiral phase plate technology [10], and range-gated imaging [11]. However, despite these advancements, the technology for fully deployable underwater lidar systems remains scarce.

Lidar deployment on underwater platforms offers great potential. First, integrated with autonomous underwater vehicles (AUVs) and remotely operated vehicles (RUVs), lidar enhances spatial positioning and target recognition, improving data accuracy in deep-sea exploration and rescue missions. Furthermore, combining lidar with sonar and imaging systems compensates for their limitations in near-field resolution and depth measurement, thereby enhancing the efficiency and accuracy of underwater searches. However, underwater lidar deployment is challenging. Firstly, water's strong absorption and scattering effects limit the effective imaging distance. To overcome this, current solutions typically increase laser pulse energy or expand the telescope aperture, but these approaches often increase system size and complicate deployment. Fortunately, by utilizing single-photon detection, the need for high laser pulse energy and large apertures is significantly reduced [12–16], enabling system miniaturization and making underwater deployment feasible [17–19]. Consequently, a partially submerged single-photon lidar imaging sensor has been proposed, where the optical transmit–receive module and array detector are submerged for operation [20].

Additionally, to achieve fast imaging, detector arrays [20] or multibeam technologies [21] are commonly employed. However, these require independent time-to-digital converters (TDCs) for each pixel, demanding high-performance computing for real-time processing [20]. To address this, multiplexing technologies such as time-division multiplexing (TDM) [22], frequency-division multiplexing [23], and spectro-temporal encoding technology [24] have been proposed for simultaneous multi-pixel

detection with a single-pixel detector. The TDM scheme based on optical fiber arrays offers a notable advantage by enabling multi-pixel detection with a simple fiber array addition to a traditional lidar, greatly simplifying the architecture [22]. Although this technical solution has been validated in atmospheric environments, it still requires further validation in more complex underwater target imaging scenarios [22]. Building on this, this work proposes and demonstrates a compact underwater lidar that utilizes fiber array TDM. Compared to existing systems, it features a compact cylindrical structure (0.18 m in diameter, 0.68 m in length) that allows full submersion and operation at depths of up to 1 km, and it offers a longer imaging distance, which reaches 10 times the optical AL. Additionally, underwater lidar imaging faces the challenge of strong scattering from particulate matter [25]. To address this issue, a background extraction and subtraction algorithm is introduced.

As shown in Figs. 1(a) and 1(c), the schematic diagram and internal structure of the underwater lidar are illustrated, respectively. The system consists of four components: a 532 nm pulsed laser, a transceiver system, a time-division multiplexing module (TDM-M), and a data acquisition system. The system uses a 532 nm pulsed laser (Keopsys, PG03D), which is generated by amplifying a 1064 nm pulsed laser in a master oscillator power amplifier configuration and then converting it to 532 nm via second-harmonic generation (SHG). The 532 nm laser features a full width at half maximum of 500 ps and a pulse repetition frequency of 1 MHz. The pulse energy is adjustable up to 1 μJ. The transmitted laser beam is adjusted to a 10 mrad divergence angle using optical lenses. The receiving system is equipped with a large-aperture achromatic fiber collimator (Thorlabs, C80SMA-A) with a focal length of 80 mm, along with a narrowband filter (0.5 nm bandwidth) placed in front of it. The backscattered signal is coupled into an array of 122 multimode fibers (MMFs) with a mode field diameter of 50 μm and a numerical aperture (NA) of 0.22. To optimize the fill factor, the 50/80 μm (core/cladding) MMFs were etched to 50/65 μm. These fibers were arranged sequentially and combined into a circular array with a diameter of 0.72 mm. The fiber array is fabricated using a silicon-based fixture made with a photolithography machine, with a precision of ±1 μm, ensuring precise arrangement and alignment of the fibers. The enlarged cross-sectional images of the fiber interfaces at positions A, B, and C, as indicated in Fig. 1(a), are shown in Fig. 1(b), further demonstrating the high-precision arrangement. As shown in Fig. 1(b) at fiber interface A, these 122 fibers are divided into two groups: the upper 61 fibers form one group, and the lower 61 fibers form the other group. The lengths of the first group of 61 fibers increase in 2 m increments: the 1st fiber is 2 m, the 2nd is 4 m, and so on, up to 122 m for the 61st fiber. The arrangement of fibers from the 1st to the 61st follows the order indicated by the arrows in Fig. 1(b). The 61 fiber outputs are combined into a circular array with a 0.5 mm diameter, with the fiber arrangement being unordered. The array is then connected to a single-pixel detector with a photosensitive area of 0.5 mm (PicoQuant, ID120). Each fiber corresponds to one pixel, enabling detection of 122 pixels, with a time delay of approximately 10 ns between adjacent pixels. Note that fabricating fiber arrays with over 122 elements is feasible, and the array can be expanded by simultaneously increasing the number of single-pixel detectors, thereby enhancing imaging resolution.

The lidar system's field of view (FOV) is 9 mrad, with each pixel covering a FOV of 0.625 mrad. The single-photon

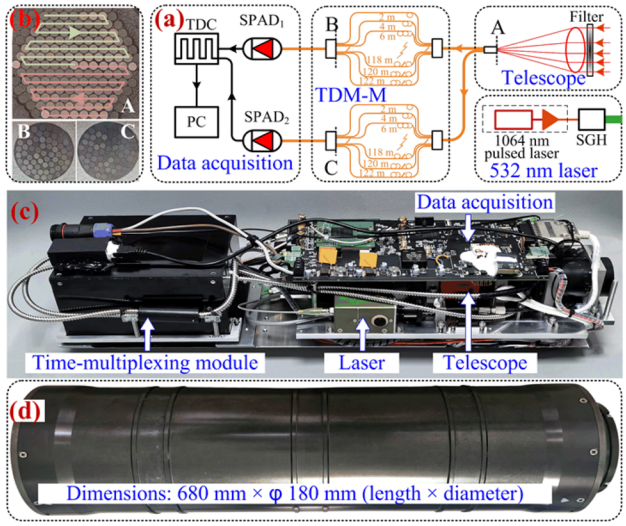

Fig. 1. (a) Schematic diagram of the lidar. SHG, second-harmonic generation; TDM-M, time-division multiplexing module; SPAD, single-photon avalanche diode; PC, personal computer. (b) Enlarged cross-sectional images of the fiber interfaces at positions A, B, and C as marked in (a). (c) Internal view of the lidar. (d) External appearance of the lidar.

avalanche diode (SPAD) has a detection efficiency of 52% at 532 nm, with a dark count rate of 100 Hz. In the electronic module, a self-developed FPGA-based function generator provides precise control signals for the laser and the custom-designed TDC, which has a root mean square jitter of 9 ps. The lidar system shown in Fig. 1(d) features a window made of sapphire glass and a casing constructed from 6061 aluminum alloy. Pressure tests show it can withstand up to 10 MPa, equivalent to 1 km depth.

To test the performance of the lidar, experimental verification was conducted at the swimming pool of Xiamen University's Xiang'an campus, which has dimensions of $50 \times 25 \times 1.9\ \mathrm{m}^3$ (length × width × depth). The lidar system was fixed using profiles and placed 1 m underwater, as shown in Fig. 2(a). It was connected by two cables: one for supplying 12 V DC power and the other for data transmission to the computer. To evaluate the lidar's resolution, including both lateral and distance resolutions, two targets were used: the striped target in Fig. 2(b) and the step target in Fig. 2(c). The striped target consists of 10 cm wide black foam strips attached to an aluminum plate, with 10 cm intervals between the strips. The step target consists of aluminum alloy steps with dimensions of $10 \times 10 \times 10\ \mathrm{cm}^3$ (length × width × height), $10 \times 10 \times 20\ \mathrm{cm}^3$, and $10 \times 10 \times 30\ \mathrm{cm}^3$, placed adjacently. To measure the beam attenuation coefficient $c(532)$ of water at 532 nm, the inherent optical properties (IOPs) measurement device (ac-s) was used, as shown in Fig. 2(d). The calibration methods for the ac-s, temperature, and salinity correction techniques and the scattering error correction for the absorption coefficient followed the protocols described in the literature [26].

As shown in Fig. 3, the aluminum plate was placed at approximately 54 m (diagonal of the pool). The signal measured by the SPAD_1 lidar is shown in Fig. 3. Figure 3(a) shows the raw data, with a sampling bin width of 160 ps. From Fig. 3(a), it is evident that the raw signal from the water includes multiple peaks (reflected signals from targets detected at each pixel), as well

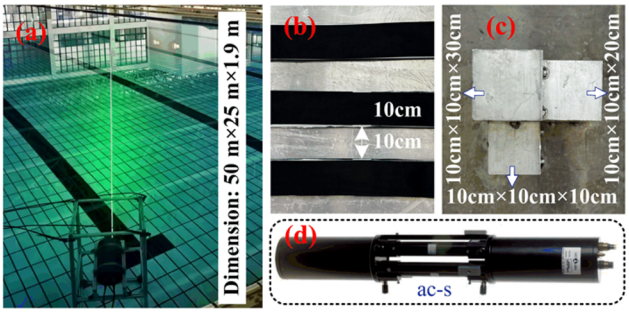

Fig. 2. Lidar testing conditions. (a) Photo of the lidar experiment in the pool. (b) Stripe target with 10 cm intervals. (c) Step target with a height interval of 10 cm. (d) Water inherent optical properties (IOPs) measurement device (ac-s).

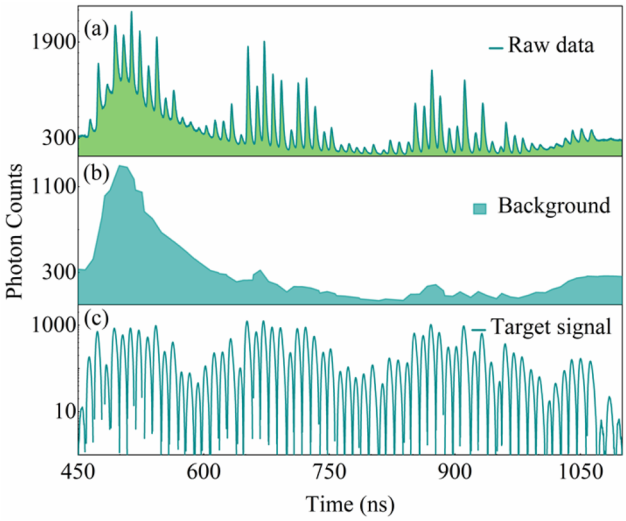

Fig. 3. Backscattered signals detected by $SPAD_1$ from a planar aluminum plate at 54 m. (a) Raw signal. (b) Extracted background scattering signal from the water column. (c) Extracted target signal.

as a background signal from scattering by water particles. This data highlights two challenges in underwater imaging: first, the rapid light attenuation caused by water (i.e., a large c), which affects the imaging distance, and second, the strong scattering signals from water particles that interfere with the extraction of the target signal. To extract the reflected signal from the target, the background scattering signal caused by water particles must first be removed. First, a window of 63 bins is set (corresponding to a time domain of 10.08 ns, which matches the 10 ns delay between two pixels), and the minimum value within the window is extracted. Then, the data is traversed with a step size of 1 bin to obtain the minimum value distribution within each 10.08 ns wide window. Finally, linear interpolation is applied to obtain the background scattering signal from water particles, as shown in Fig. 3(b). The target reflected signal can be obtained by subtracting the water scattering background signal shown in Fig. 3(b) from the raw signal shown in Fig. 3(a), as illustrated in Fig. 3(c).

Next, the underwater target was replaced with the step target shown in Fig. 2(c), placed at distances of 19.5 m, 29.5 m, 39 m, and 54.5 m from the lidar, with imaging results shown in Fig. 4. Before imaging the underwater targets, the lidar signal

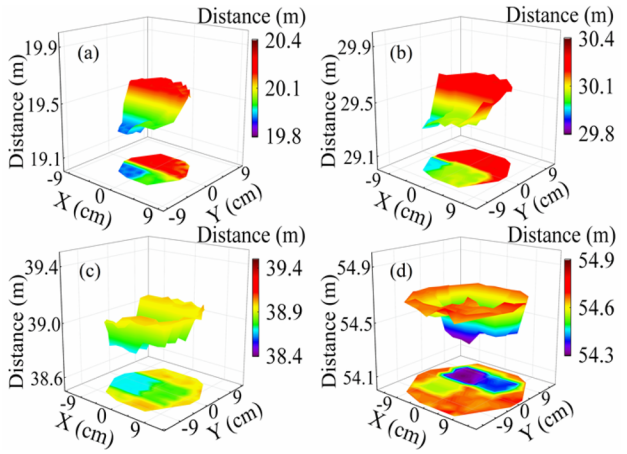

Fig. 4. Imaging results of the step target at different distances: (a) 19.5 m, (b) 29.5 m, (c) 39 m, and (d) 54.5 m.

was calibrated using a known distance plane aluminum plate in the air to correct for response differences between pixels and relative time delays. Additionally, to extract the distance of each pixel (i.e., the peak position of the reflected signal of the target shown in Fig. 3(c)), the islocalmax function in MATLAB was used to extract the peak values of the reflected target signal. Due to the small FOV of the lidar, comprehensive imaging of the entire step is challenging at shorter distances, as shown in Fig. 4(a)–4(c). However, at a target distance of 54.5 m, as shown in Fig. 4(d), comprehensive imaging of all three steps can be achieved. During the lidar imaging process, the $c(532)$, measured by the ac-s, was 0.19 m^{-1}, corresponding to an optical AL of 5.3 m, where AL is the inverse of $c(532)$. From the analysis of the backscattered signals, it is observed that for the aluminum alloy step target, the imaging distance of the underwater lidar is approximately 10 times the AL. Statistical analysis of the three 10 cm high steps shown in Fig. 4(d) revealed average heights of 30.1 cm, 22 cm, and 9.1 cm, with a standard deviation of less than 2 cm for each step, confirming the excellent depth resolution capability of the underwater single-photon lidar.

To test the lateral resolution capability of the lidar, the next experiment used the striped target shown in Fig. 2(b). When the striped target was placed at 54.5 m, the backscattered signal detected by the lidar is shown in Fig. 5(a). The target reflected signal extracted using the above method is shown in Fig. 5(b). When the underwater lidar hits the black foam of the striped target, the target reflected signal is very weak due to the light absorption by the black foam. However, when the laser hits the aluminum alloy plate, the target reflected signal is significantly stronger, as seen in the latter part of the signal in Fig. 5(b). To obtain the stripe image, an aluminum alloy plate was first used at the same position (54.5 m) to measure the target signal from different pixels on the aluminum alloy plate. Then, the target signal of the striped target was divided by the target signal of the flat plate to obtain the normalized signal shown in Fig. 5(c). When the lidar measures the black foam, the normalized signal is weak; when it measures the aluminum alloy plate, the normalized signal is close to 1. When the measured area contains both the black foam and the aluminum alloy plate, the normalized signal weakens. For example, in the case shown in Fig. 5(c), the normalized signal is approximately 0.67. Based on the normalized signal, regions with a value greater than 0.5 are identified

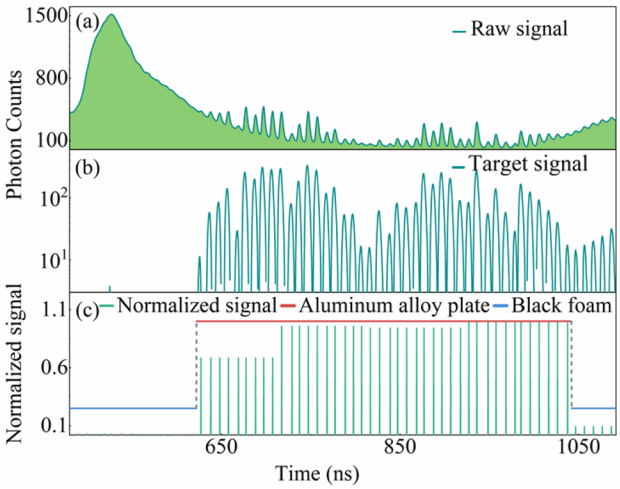

Fig. 5. Signals of the stripe target located 54.5 m away, detected by $SPAD_1$. (a) Raw data. (b) Extracted target signal. (c) Normalized signal, obtained by dividing the signal of each pixel on the striped target by the corresponding pixel signal measured from the aluminum alloy plate at the same distance (54.5 m).

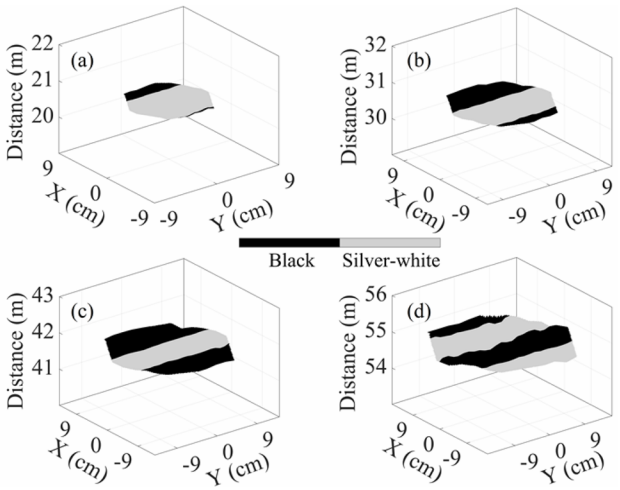

Fig. 6. Imaging results of the stripe target at different distances: (a) 20 m, (b) 30 m, (c) 41 m, and (d) 54.5 m.

as the aluminum alloy plate, while regions with a value less than 0.5 are identified as the black foam.

During the testing phase, the striped target was placed at distances of 20 m, 30 m, 41 m, and 54.5 m. The imaging results are shown in Fig. 6. According to data analysis, the measured width of the aluminum alloy stripe at 54.5 m, shown in Fig. 6(d), is 9.7 cm, which is close to the actual stripe width of 10 cm, thus verifying that the lidar has high lateral resolution capability.

In conclusion, a compact single-photon imaging underwater lidar, capable of withstanding pressures exceeding 10 MPa, is proposed and demonstrated. To minimize the size of the lidar, the prototype employs a fiber-array-based TDM technique, enabling underwater small-target imaging with only two single-pixel detectors and a two-channel TDC. To extract the target signal, an algorithm for background extraction and subtraction, caused by particle scattering in the water, is proposed. Through pool experiments, it was demonstrated that the lidar can detect aluminum alloy targets at a distance approximately 10 times the AL, achieving cm-level lateral and depth resolutions. Additionally, in the TDM scheme, the 10 ns pixel ambiguity range is 1.5 m, which may cause signal aliasing when the target depth exceeds 1.5 m or with multiple targets. Future work will involve developing algorithms or integrating other detection methods to address this issue. Furthermore, a scanning unit will be added to the lidar, overcoming challenges in motion compensation, image stitching, and real-time data processing, thereby enabling underwater target imaging within a wide FOV. Additionally, by mounting this miniaturized lidar on an underwater maneuverable platform, it is expected to play a key role in blue carbon seagrass surveys, as well as coral and other marine ecosystem investigations.

Funding. National Natural Science Foundation of China (42476184); Natural Science Foundation of Xiamen, China (3502Z202473033).

Acknowledgment. The authors would like to thank Zhifeng Yang and Zaifa Lin for their assistance with the assembly of the lidar system and field experiments.

Disclosures. The authors declare no conflicts of interest.

Data availability. The data that support the findings of this study are available from the corresponding author upon reasonable request.

REFERENCES

1. H. Johannsson, M. Kaess, B. Englot, *et al.*, in *2010 IEEE/RSJ International Conference on Intelligent Robots and Systems, (IEEE)* (2010), pp. 4396–4403.
2. Y. Huang, F. Yuan, F. Xiao, *et al.*, IEEE J. Oceanic Eng. **48**, 903 (2023).
3. J. E. Hughes Clarke, L. A. Mayer, and D. E. Wells, Marine Geophysical Researches **18**, 607 (1996).
4. T. Guerneve, K. Subr, and Y. Petillot, J. Field Rob. **35**, 890 (2018).
5. Y. Xie, N. Bore, and J. Folkesson, IEEE J. Oceanic Eng. **48**, 372 (2023).
6. H. Zhao, X. Xu, Z. Qian, *et al.*, Opt. Laser Technol. **148**, 107749 (2022).
7. Y. Li, M. Chen, J. Qi, *et al.*, Opt. Express **31**, 38457 (2023).
8. M. Fang, Y. Xue, C. Ji, *et al.*, Appl. Opt. **61**, 7401 (2022).
9. G. Li, Q. Zhou, G. Xu, *et al.*, Opt. Laser Technol. **142**, 107234 (2021).
10. Y. Liao, S. Yang, X. Lin, *et al.*, Opt. Laser Technol. **159**, 109008 (2023).
11. M. Wang, X. Wang, Y. Zhang, *et al.*, Opt. Express **29**, 7630 (2021).
12. A. Halimi, A. Maccarone, R. A. Lamb, *et al.*, IEEE Trans. Comput. Imaging **7**, 961 (2021).
13. A. Halimi, A. Maccarone, A. McCarthy, *et al.*, IEEE Trans. Comput. Imaging **3**, 472 (2017).
14. J. Wang, W. Hao, S. Chen, *et al.*, Opt. Express **31**, 30588 (2023).
15. M. Shangguan, H. Xia, C. Wang, *et al.*, Opt. Lett. **42**, 3541 (2017).
16. M. Shangguan, H. Xia, C. Wang, *et al.*, Opt. Express **24**, 19322 (2016).
17. M. Shangguan, Z. Yang, Z. Lin, *et al.*, IEEE Geosci. Remote Sensing Lett. **20**, 1 (2023).
18. M. Shangguan, Z. Yang, M. Shangguan, *et al.*, Appl. Opt. **62**, 5301 (2023).
19. M. Shangguan, Z. Yang, Z. Lin, *et al.*, Opt. Lett. **49**, 626 (2024).
20. A. Maccarone, K. Drummond, A. McCarthy, *et al.*, Opt. Express **31**, 16690 (2023).
21. Z. Li, E. Wu, C. Pang, *et al.*, Opt. Express **25**, 10189 (2017).
22. M. Shangguan, Y. Liang, Y. Li, *et al.*, Appl. Phys. Lett. **124**, 1 (2024).
23. T. Zheng, G. Shen, Z. Li, *et al.*, Photonics Res. **7**, 1381 (2019).
24. Z. Zang, Z. Li, Y. Luo, *et al.*, APL Photonics **7**, 1 (2022).
25. Z. Zhang, S. Chen, J. Wang, *et al.*, IEEE Photonics Technol. Lett. **35**, 253 (2023).
26. W. S. Pegau, D. Gray, and J. R. V. Zaneveld, Appl. Opt. **36**, 6035 (1997).